Journal of Physics and Chemistry of Solids 167 (2022) 110785

Contents lists available at ScienceDirect

Journal of Physics and Chemistry of Solids

journal homepage: www.elsevier.com/locate/jpcs

The effect of copper and iron adsorption on the catalytic performance of alumina nanofiber / nanodiamond composite in sensing applications

Nikita O. Ronzhin [a], Ekaterina D. Posokhina [a], Elena V. Mikhlina [b], Nikolai P. Shestakov [c], Ivan V. Nemtsev [c,d,e], Vladimir S. Bondar [a], Ilya I. Ryzhkov [b,e,*]

[a] Institute of Biophysics SB RAS, Akademgorodok 50/50, 660036, Krasnoyarsk, Russia
[b] Institute of Computational Modelling SB RAS, Akademgorodok 50/44, 660036, Krasnoyarsk, Russia
[c] Kirensky Institute of Physics SB RAS, Akademgorodok 50/38, Krasnoyarsk, 660036, Russia
[d] Federal Research Center KSC SB RAS, Akademgorodok 50/38, Krasnoyarsk, 660036, Russia
[e] Siberian Federal University, Svobodny 79, Krasnoyarsk, 660041, Russia

ARTICLE INFO

Keywords:
Nanodiamonds
Alumina nanofibers
Indicator system
Copper ions
Iron ions
Phenol detection

ABSTRACT

Phenolic compounds are common environmental pollutants, which are used in many industries and contaminate water environment due to industrial wastewater discharge. Presently, there is an increasing demand for the development and improvement of inexpensive, easy-to-use analytical tools for in-situ detection of phenolic compounds. In this work, we investigate the effect of adsorption of Cu^{2+} and Fe^{2+} ions on the catalytic activity of a composite material based on alumina nanofibers (ANF) and detonation nanodiamonds (DND) in the co-oxidation of phenols with 4-aminoantipyrine in the presence of hydrogen peroxide. We have found more than two-fold increase of the catalytic activity for ANF + DND + Cu composite, while the activity of ANF + DND + Fe composite is found to decrease by several times in comparison with the original ANF + DND material. The results of FTIR analysis indicate that the adsorption of iron ions occurs with the formation of hydroxide surface groups and hydrogen bonds, which apparently block their catalytic activity in the Fenton redox cycle. The higher catalytic performance of AND + DND composite functionalized with copper ions makes it possible to detect two times lower concentrations of analytes (phenol and 4-chlorophenol) in comparison with the original composite. It is shown that the AND + DND + Cu composite provides a linear yield of the co-oxidation reaction product in a wide range of analyte concentrations (0.25–100 μM for phenol and 0.5–25 μM for 4-chlorophenol). Model experiments demonstrate the applicability of copper-functionalized composite as a reusable sensor for the determination of phenol in aqueous samples.

1. Introduction

As a result of industrial activities and agricultural production, a number of different pollutants are constantly released into the environment. Phenol and chlorophenol compounds (such as 2-chlorophenol, 4-chlorophenol, and 2,4-dichlorophenol) are common environmental pollutants from the production of paper, resins and plastics, dyes and textiles, and pesticides [1–5]. These pollutants are present in industrial wastewater and end up in natural and drinking water, which is extremely dangerous for the environment, animals, and humans. Phenolic compounds are resistant to natural decomposition, highly toxic, carcinogenic and mutagenic, easily absorbed by animals and humans through the skin and mucous membranes affecting a variety of organs and tissues [6–8]. Due to its toxicological and environmental effects, phenol is included in the list of priority pollutants by many countries with emission limit for industrial wastewater currently set below 0.5 mg/l [9,10].

Currently, chromatographic [11,12], electrochemical [13–15], chemiluminescent [16], fluorescent [17], and spectrophotometric [18] methods are used for the detection of phenols. At the same time, there is an increasing demand for new methods for the detection of phenolic compounds allowing *in situ* testing of contaminants.

Among the existing analytical methods, colorimetric analysis has attracted significant attention because it requires simple instrumentation (e.g. a UV–visible spectrophotometer) and screening analysis (e.g. camera or naked eye). This analysis is traditionally performed with the

* Corresponding author. Institute of Computational Modelling SB RAS, Akademgorodok 50/44, 660036, Krasnoyarsk, Russia.
E-mail address: rii@icm.krasn.ru (I.I. Ryzhkov).

https://doi.org/10.1016/j.jpcs.2022.110785
Received 2 March 2022; Received in revised form 13 April 2022; Accepted 6 May 2022
Available online 11 May 2022
0022-3697/

help of enzymes, which are ideal biocatalysts with high efficiency and specificity. However, they have low operational stability, high cost as well as difficulties in recovery and reuse. To eliminate these shortcomings, enzymes are immobilized on various carriers (matrices) including nanomaterials [19–23].

It should be noted that immobilization on carriers can increase the resistance of enzymes and increase the possibility of their reuse for analysis. However, the implementation of this procedure requires careful and inventive design conditions since enzymes can be easily damaged and even inactivated during the immobilization process. In this regard, nanosized materials with enzyme-like properties (nanozymes) have been of considerable interest to researchers in recent years as an alternative option. To date, a large number of nanostructured materials are known that exhibit enzyme-like activity: magnetic Fe_3O_4 nanoparticles [24], platinum nanoparticles [25], cerium oxide nanoparticles [26], gold nanoparticles [27], copper oxide nanoparticles [28], graphene oxide [29], and single-walled carbon nanotubes [30]. In comparison with enzymes, nanozymes have a number of advantages: better stability, lower cost, and easier control of catalytic properties. A number of studies have shown that nanozymes hold great promise for the efficient detection of phenolic compounds [31–35].

In addition to sp^2–nanocarbon [29,30], sp^3–nanocarbon/nanodiamonds are used in the fabrication of sensors. When designing sensors for detection of phenolic compounds, nanodiamonds are mainly employed to improve the performance of glassy carbon electrodes because reaction by-products lead to fouling of their surface and the corresponding decrease of accuracy and lifespan. In particular, nanodiamonds provided high chemical resistance to glassy carbon electrode in a reusable sensor for the determination of hydroquinone and catechol [36] as well as bisphenol A [37]. Nanodiamonds were also employed for improvement of electrochemical response of electrode sensor for hydroquinone and catechol detection [38]. Another application of nanodiamonds is the fabrication of supports for enzyme immobilization. When constructing a biosensor for catechol detection, diamond nanoparticles were utilized to obtain a composite starch matrix for immobilization of tyrosinase [39]. At the same time, the sensor systems, where nanodiamonds would act as a main sensor element (catalyst), have not been studied in the literature except the works of the present authors mentioned below.

Earlier, we found the enzyme-like activity of detonation nanodiamonds (DND) in the co-oxidation reaction of phenol with 4-aminoantipyrine (AAP) in the presence of hydrogen peroxide. It was revealed that the catalytic effect of DND is realized due to the presence of copper and iron impurities on their surface [40]. In the subsequent work [41], we first used the alumina nanofibers (ANF) to prepare the host matrix for fixation of DND. It allowed us to create a sensor composite for the colorimetric determination of phenol in an aqueous medium. The employed nanofibers had a diameter of 10–20 nm and possessed an extremely high aspect ratio (the length of nanofibers is in the cm range) and a high specific surface area (about 155 m^2/g) [42–44].

In this work, we first investigate the effect of iron and copper ions adsorption on the catalytic activity of ANF + DND composite in the co-oxidation reaction of phenols with 4-aminoantipyrine. The adsorption kinetics is studied and adsorption mechanisms are discussed and analyzed on the basis of elemental analysis and FTIR spectroscopy. It demonstrated that the sensor performance of the original composite in the detection of phenols can be enhanced by its functionalization with copper ions.

2. Materials and methods

2.1. Materials and chemicals

To prepare a composite material, we use detonation nanodiamonds (DND) with an average cluster size of 70 nm and high colloid stability in aqueous suspensions. The commercial nanodiamonds of detonation synthesis (OOO Real-Dzerzhinsk, Russia) are treated with sodium chloride [45], which makes it possible to additionally purify nanoparticles from surface impurities and, thereby, increase their colloidal stability in dispersion media. Nafen™ alumina nanofibers (ANF) with a fiber diameter of 10–15 nm and a length of up to several cm (ANF Technology, Estonia) are used as a host matrix for DND.

Iron and copper sulfates ($FeSO_4$, $CuSO_4$) (Reakhim, Russia) are employed to prepare the adsorbate solutions. 4-AAP (1-phenyl 2,3-dimethyl 4-aminopyrazolone) (Reakhim, Russia), phenol and 4-chlorophenol (Fluka, Germany), 3% hydrogen peroxide solution (Galeno Pharm™, Russia) are used for the oxidative azo coupling reaction. All chemicals are of reagent grade purity and deionized (DI) water is used to prepare all solutions.

2.2. Composite fabrication

The methodology of obtaining the composite material ANF + DND is described in details in our previous work [41]. Briefly, a weighed portion of ANF (0.5 g) is added to a volume of DI water, and the mixture is incubated for 30 min with constant stirring on a magnetic stirrer. Then the resulting suspension is ultrasonically treated (Sonics & Materials VC-505.22 kHz, USA) to increase the colloidal stability of nanomaterial. The composite is obtained by mixing suspensions of DND and ANF in a ratio of 1 : 5 (w: w) followed by incubation of the resulting mixture for 15 min at the temperature of 32 °C with constant stirring on a magnetic stirrer. After that, the mixture is vacuum filtered through a PTFE filter with a pore diameter of 0.6 μm, which allows obtaining a 40 mm disk of the composite material. The disc is subjected to heat treatment (Spark-Don Microterm 95, Russia) at 300 °C for 4 h to give it structural stability. The discs of smaller diameter (5 mm) are cut from the original 40 mm discs with the help of a laser (Sharp-Mark-30SM Fiber smart, USA) and used in the further experiments. Similar discs cut from the ANF matrix are used as controls in comparative studies.

2.3. Adsorption experiments

The effect of pH on ion adsorption is evaluated over the pH range from 4 to 9. The 0.1 M HCl and 0.1 M NaOH solutions are used as acid and base titrants.

Adsorption kinetic studies are conducted at the initial pH = 7 and the initial Cu^{2+} and Fe^{2+} concentration of 50 mM. A composite disc or an ANF matrix disc is placed in the test tubes containing 0.6 ml of copper sulfate (or iron sulfate) solution, and the samples are incubated at a temperature of 22 ± 2 °C with constant stirring at 150 rpm on an Orbital Shaker OS-10 (BIOSAN, Latvia). Changes in the optical density of solutions are evaluated every 5 min using a UV-1800 spectrophotometer (Shimadzu, Japan) at the wavelength of 295 nm for $FeSO_4$ and 810 nm for $CuSO_4$. The amount of adsorbed ions is calculated using the equation

$$q = \frac{(C_0 - C)V}{m}, \quad (1)$$

where q is the amount of adsorbed metal ions (mg/g), C_0 is the concentration of metal ions in the solution before adsorption (mg/ml), C is the concentration of metal ions in the solution after adsorption (mg/ml), m is the mass of the adsorbent (g), and V is the volume of the adsorbate solution (ml).

To obtain the adsorption isotherms, we use solutions with Fe^{2+} and Cu^{2+} ion concentrations of 6.25, 12.5, 25, and 50 mM. The experiments are carried out at pH = 7 and the temperature of 22 ± 1 °C. A composite disc or an ANF matrix disc is placed in the test tubes containing 0.6 ml of solutions with different concentrations of ions and incubated with constant stirring until adsorption equilibrium is reached according to the spectrophotometric data as described above. The adsorption capacities are calculated using Eq. (1).

2.4. Characterization of samples

The SEM images are obtained by the ultra-high resolution scanning electron microscope S–5500 (Hitachi, Japan) operating at 3 kV and 10 kV. Before examination, the samples of ANF matrix and ANF-DND composite are coated with platinum by low vacuum desk-top coater for SEM analysis EM ACE200 (Leica, Austria) during 1 min at the current of 25 mA and the pressure of 8×10^{-6} bar in argon atmosphere. It is done to prevent charging of dielectric nanofibers in the SEM.

A comparative analysis of the elemental composition of the composite samples and the ANF matrix before and after the adsorption of ions is performed on a TM4000 Plus II tabletop microscope (Hitachi, Japan) at an acceleration voltage of 20 kV.

Fourier transform infrared absorption (FTIR) spectra are recorded with the VERTEX 70 (Bruker Optik GMBH) spectrometer in the spectral region of 370 ÷ 4000 cm^{-1} with the spectral resolution if 4 cm^{-1}. The FTIR spectrometer is equipped with a ceramic Globar as a MIR light source, a wide band KBr beam splitter, and RT–DLaTG as a detector (Bruker Optik GMBH). To obtain the spectra, the tablet samples containing ANF, ANF + Fe/Cu, ANF + DND, ANF + DND + Fe/Cu are prepared as follows: 0.001 g of sample powder is thoroughly ground with 0.140 g of KBr and subjected to cold pressing at 10,000 kg. The obtained tablets are of 0.5 mm thick and 13 mm in diameter and have the weight of 0.140 g.

2.5. Catalytic activity mechanisms and measurement

The determination of phenol is based on the metal-catalysed hydrogen peroxide decomposition followed by the co-oxidation of phenol and 4-aminoantypirine to quinoneimine dye. At the first step, the hydrogen peroxide is activated by the Fe^{2+} ion to produce hydroxide radical $HO^{\bullet}$ (the Fenton reaction) with subsequent reduction of oxidized Fe^{3+} intoFe^{2+} [46–48]:

$$Fe^{2+} + H_2O_2 \rightarrow Fe^{3+} + HO^{\bullet} + OH^{-}, \quad (2)$$

$$Fe^{3+} + H_2O_2 \rightarrow Fe^{2+} + HO_2^{\bullet} + H^{+}.$$

An analogues redox cycle on the basis of Cu^{2+} ions is described by [42,44].

$$Cu^{2+} + H_2O_2 \rightarrow Cu^{+} + HO_2^{\bullet} + H^{+}, \quad (3)$$

$$Cu^{+} + H_2O_2 \rightarrow Cu^{2+} + HO^{\bullet} + OH^{-}.$$

At the second step, the attack of phenol by the hydroxyl radical produces the phenoxy radical

$$2PhOH + 2HO^{\bullet} \rightarrow 2PhO^{\bullet} + 2H_2O.$$

Then the antipyril radical is generated

$$PhO^{\bullet} + AmNH_2 \rightleftharpoons PhOH + AmNH^{\bullet}$$

and reacts with another phenoxy radical the obtain a pyrazolone derivative

$$PhO^{\bullet} + AmNH^{\bullet} \rightarrow AmNHPhO,$$

which is finally converted into quinoneimine dye by the action of hydrogen peroxide [49,50].

$$AmNHPhO + H_2O_2 \rightarrow Dye + 2H_2O.$$

The catalytic activity of the samples (ANF matrix and ANF + DND composite disks) before and after functionalization with Cu^{2+} or Fe^{2+} ions is evaluated using the above-described oxidative azo coupling reaction. The reaction is carried out in 0.6 ml of DI water containing various concentrations of phenol (or 4-chlorophenol), 0.49 mM 4-AAP, and 8.8 mM H_2O_2. The reaction is initiated by adding a sample to the volume of reaction mixture, after which the samples are incubated at 50 °C for 10 min with constant stirring. After that, the liquid part of the samples is taken and the amount of resulting colored reaction product directly proportional to the analyte content in the test sample is determined spectrophotometrically (UV-1800) at the wavelength of 506 nm. Each measuring experiment of catalytic activity is performed in quintuplicate. Error bars are generated as a standard deviation of the mean from 5 replicates.

3. Results and discussion

3.1. Composite morphology

The SEM images of ANF matrix and ANF + DND composite as well as top views of 5 mm discs prepared from these materials are presented in Fig. 1. The results of microscopic analysis show that the composite has a network structure, in which nanodiamonds are distributed over the surface of alumina nanofibers in the form of clusters with the size of 10–20 nm (Fig. 1b).

3.2. Influence of pH on adsorption

The study of pH effect on the adsorption shows that the amount of ions adsorbed on the ANF + DND composite increases, on average, by a factor of 2 with the increase of pH from 4 to 7 for both Cu^{2+} and Fe^{2+} ions (Fig. 2). The highest adsorption for both ions is observed in DI water at neutral pH. Under these conditions, 1.4 times more Fe^{2+} ions than Cu^{2+} ions are adsorbed on a composite sample from ionic solutions with equal initial concentrations (50 mM). The shift of pH values to the alkaline region for both ionic solutions leads to their clustering [51] with the formation of insoluble flocculent precipitates of $Cu(OH)_2$ and $Fe(OH)_2$. This prevents adsorption and makes it impossible to obtain the correct data on the amount of ions bound to the composite under alkaline conditions.

3.3. Adsorption kinetics

We have experimentally studied the adsorption kinetics of Cu^{2+} and Fe^{2+} ions on the ANF + DND composite and ANF matrix and fitted the experimental data using theoretical models to determine the reaction order.

Fig. 3 (a) and (b) show the adsorption curves for iron and copper ions, respectively, obtained in 50 mM sulfate solutions. In both cases, the amount of adsorbed ions increases rapidly during the first 20 min, and after that the process slows down and reaches the stationary state. The equilibrium adsorption times for Cu^{2+} and Fe^{2+} ions can be estimated as 45 min and 60 min, respectively.

The theoretical description of adsorption kinetics is performed with the help of two models. The pseudo-first-order kinetic model is given by

$$q_t = q_e(1 - \exp(-k_1 t)), \quad (4)$$

where k_1 is the first-order rate constant (min^{-1}), t is the adsorption time (min), and q_e and q_t are the equilibrium adsorbance and the adsorbance at reaction time t, respectively (mg/g). The pseudo-second-order kinetic model can be expressed as

$$q_t = \frac{k_2 q_e^2 t}{1 + k_2 q_e t}, \quad (5)$$

where k_2 is the second-order rate constant (g mg^{-1} min^{-1}). The kinetic parameters for both models obtained from fitting the experimental data are presented in Table 1.

It can be seen that the equilibrium adsorbance is better described by the pseudo-first-order model (4) than by the pseudo-second-order model (5), see Fig. 3. This is supported by the fact the squared correlation coefficient for model (4) is higher than that for model (5), see Table 1. The first order kinetic process corresponds to reversible ion/surface

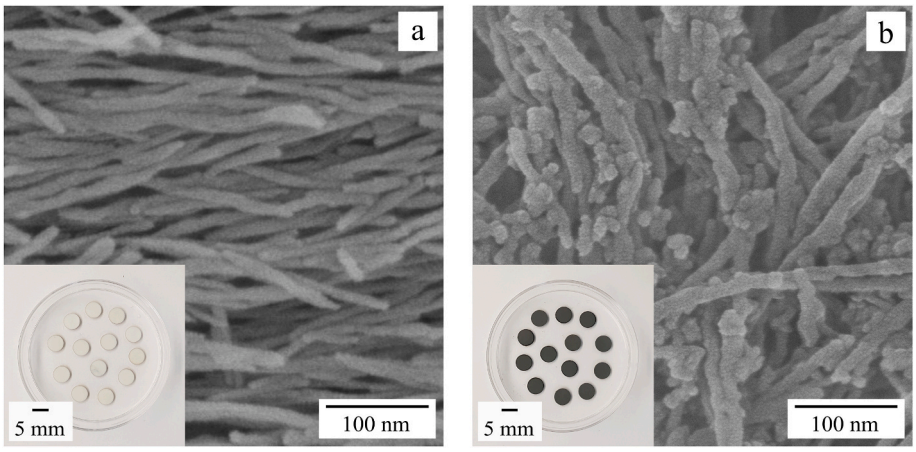

Fig. 1. Top view of disks and SEM images of ANF matrix (a) and ANF + DND composite (b).

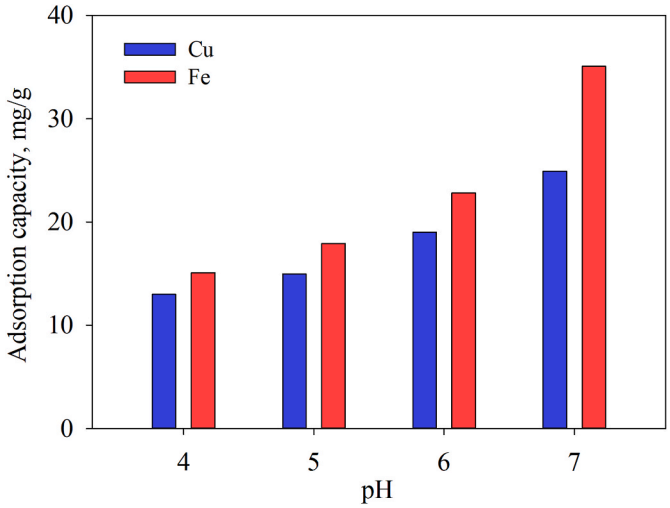

Fig. 2. Effect of initial solution pH values on Cu^{2+} and Fe^{2+} adsorption capacity of the composite.

interactions with the equilibrium being established between liquid and solid phases, while the second order kinetic model assumes that the rate-limiting step is determined by chemicals interactions of ions with the surface [52].

3.4. Adsorption isotherms

Measurement of adsorption isotherms with subsequent approximation of data by a mathematical model makes it possible to evaluate the features of the adsorbate binding to the adsorbent and to calculate its maximum load (adsorption capacity) with the adsorbate. The experimental data obtained during the adsorption of Cu^{2+} and Fe^{2+} ions on the ANF + DND composite and the ANF matrix are shown in Fig. 4.

To approximate the obtained data, the Langmuir model is used

$$q_e = \frac{q_m K_L C_e}{K_L C_e + 1} \tag{6}$$

where q_e is the equilibrium adsorbance (mg/g), q_m (mg g^{-1}) is the maximum adsorption capacity of metal ion per unit weight of adsorbent, C_e is the equilibrium concentration of metal ions (mg/L); K_L (L/mg) is Langmuir constant related to the maximum adsorption capacity and energy of adsorption.

The fitting of Eq. (6) to the adsorption data for both ions on the ANF + DND composite and ANF matrix shows that the Langmuir model describes the data quite well with a high value of the squared correlation

Table 1
The kinetic parameters for Cu^{2+} and Fe^{2+} adsorption on the ANF matrix and ANF + DND composite.

Model	Parameters	Cu^{2+}		Fe^{2+}	
		ANF	ANF + DND	ANF	ANF + DND
Pseudo-first-order	k_1 (min^{-1})	0.0835	0.0974	0.0670	0.0654
	q_e (mg g^{-1})	19.12	22.18	30.88	36.18
	R^2	0.998	0.994	0.997	0.998
Pseudo-second-order	k_2 (g mg^{-1} min^{-1})	0.0056	0.0061	0.0025	0.0020
	q_e (mg g^{-1})	21.40	24.46	35.39	41.62
	R^2	0.984	0.988	0.989	0.988

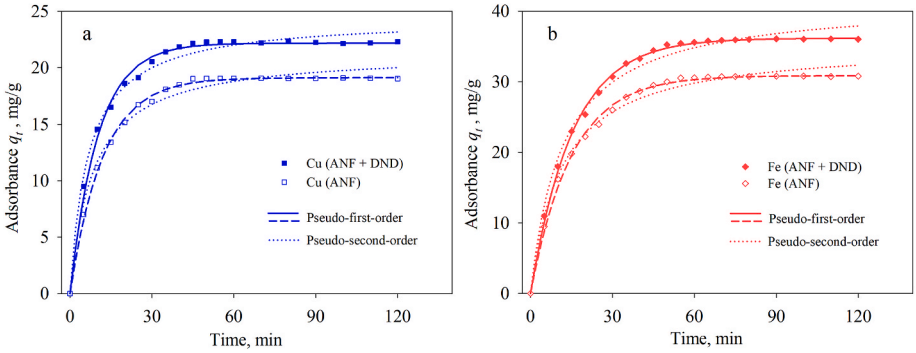

Fig. 3. The dependence of adsorbance on time for Cu^{2+} (a) and Fe^{2+} (b) ions and the fitted curves on the basis of pseudo first- and second-order models.

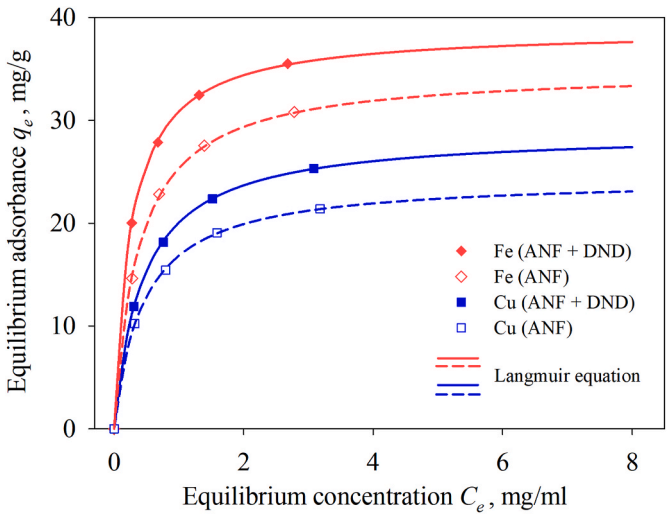

Fig. 4. The adsorption data for Cu^{2+} and Fe^{2+} ions on the ANF + DND composite and ANF matrix and its description by the Langmuir isotherm.

$R^2 = 0.999$ (Fig. 4 and Table 2). This suggests that Cu^{2+} and Fe^{2+} ions are adsorbed on the heterogeneous surface of ANF + DND composite (or ANF matrix) in the form of a monolayer interacting with their functional groups (binding sites). From the comparative data presented in Figs. 3 and 4, it follows that the amount of Cu^{2+} and Fe^{2+} ions adsorbed on the ANF + DND composite is higher by 12–15% than that adsorbed on the ANF matrix. This allows us to conclude that the incorporation of DND particles with chemically active surface sites into the ANF matrix increases its adsorption capacity for iron and copper ions.

3.5. Adsorption mechanisms

On the surface of alumina nanofibers, the following amphoteric dissociation reactions of Al − OH groups occur [53–55]:

$$\begin{aligned} &Al-O^- + H^+ \rightleftharpoons Al-OH, \\ &Al-OH + H^+ \rightleftharpoons Al-OH_2^+. \end{aligned} \quad (7)$$

The surface charge of alumina nanofibers is positive for pH < 9 and negative for pH > 9 [41]. Thus, the positively charged surface groups $Al-OH_2^+$ and negatively charged surface groups $Al-O^-$ are dominant for pH < 9 and pH > 9, respectively. However, the concentrations of neutral Al − OH surface groups is typically an order of magnitude higher in comparison with that of positively and negatively charged surface groups.

On the surface of nanodiamonds, the carboxyl surface groups can dissociate according to [41,56,57].

$$-COOH \rightleftharpoons COO^- + H^+. \quad (8)$$

The nanodiamonds are negatively charged over a wide range of pH (in particular, from 4 to 10 [41]), thus the equilibrium in reaction (8) is shifted to the right.

The mechanism of metal ions adsorption on the surface of alumina nanofibers is described by the series of complexation reactions [51,58,59]. The metal cations can exchange with the hydrogen ions according to

$$\begin{aligned} &Al-O^- + M^{2+} \rightleftharpoons Al-O^-M^{2+}, \\ &Al-OH + M^{2+} \rightleftharpoons Al-O^-M^{2+} + H^+, \\ &Al-OH_2^+ + M^{2+} \rightleftharpoons Al-O^-M^{2+} + 2H^+. \end{aligned} \quad (9)$$

Another possibility is the formation of surface complexes, where the metal cation is coordinated with two $Al-O^-$ groups:

$$\begin{aligned} &2Al-O^- + M^{2+} \rightleftharpoons (Al-O^-)_2M^{2+}, \\ &2Al-OH + M^{2+} \rightleftharpoons (Al-O^-)_2M^{2+} + 2H^+, \\ &2Al-OH_2^+ + M^{2+} \rightleftharpoons (Al-O^-)_2M^{2+} + 4H^+. \end{aligned} \quad (10)$$

The bonding with a single surface oxygen and OH^- group can also occur

$$\begin{aligned} &Al-O^- + M^{2+} + H_2O \rightleftharpoons Al-OMOH + H^+, \\ &Al-OH + M^{2+} + H_2O \rightleftharpoons Al-OMOH + 2H^+, \\ &Al-OH_2^+ + M^{2+} + H_2O \rightleftharpoons Al-OMOH + 3H^+. \end{aligned} \quad (11)$$

The adsorption of metal cations on the surface of nanodiamonds is described by similar complexation reactions [60,61].

$$-COOH + M^{2+} \rightleftharpoons COO^-M^{2+} + H^+, \quad (12)$$

$$2(-COOH) + M^{2+} \rightleftharpoons (COO^-)_2M^{2+} + 2H^+, \quad (13)$$

$$-COOH + M^{2+} + H_2O \rightleftharpoons COOMOH + 2H^+. \quad (14)$$

3.6. Elemental analysis

The results of elemental analysis of DND powder, ANF matrix, and ANF + DND composite before and after adsorption of Cu^{2+} and Fe^{2+} ions are shown in Fig. 5. It reveals the presence of Cu and Fe on the surface of the DND nanoparticles in amounts of 0.65 and 0.43 wt %, respectively. The analysis of surface and bulk of the ANF + DND composite shows that it contains a slightly smaller amounts of Cu and Fe, but their ratio remains the same as in the DND powder. The analysis of ANF matrix, as expected, reveals Al and O, but also indicates a small amount of C (about 5 wt%), which is probably associated with the inevitable contamination of the nanofiber surface with carbon from the environment during the preparation of ANF matrix discs.

Elemental analysis of the ANF matrix and ANF + DND composite after adsorption of ions reveals the increase of their amount on the surface and in the bulk of samples (Fig. 5). The average (surface + bulk) content of iron and copper ions in the ANF matrix after adsorption is 0.94 and 1.33 wt %, respectively. The average increase of iron and copper ions in the ANF + DND composite after adsorption is 1.13 and 1.47 wt %, respectively. The copper content in the ANF + DND sample increases by a factor of 4.5, while the iron content becomes larger by a factor of 5.2 after the functionalization.

Elemental analysis also indicates that the carbon content inside the ANF + DND composite is 2.2 times higher than on its surface, while the oxygen content, on the contrary, is two times lower. The higher content of carbon is obviously due to the higher amount of nanodiamonds in the composite bulk. The lower oxygen content in the bulk can be associated with a larger amount of nanodiamonds, which cover the surface of alumina nanofibers and are chemically bonded to them. We have previously found that during heat treatment of the composite at 300 °C, an intensive release of CO_2 occurs from the surface of nanodiamonds [41], and the oxygen content in the sample decreases. After heat treatment, the composite surface is again oxidized by the atmospheric oxygen, but its bulk is less prone to the oxidation processes. Note that the elemental analysis of composite bulk was performed immediately after disc splitting to obtain its cross-section.

Table 2
Langmuir isotherm model constants and correlation coefficients for Cu^{2+} and Fe^{2+} adsorption on the ANF matrix and ANF + DND composite.

Parameters	Cu^{2+}		Fe^{2+}	
	ANF	ANF + DND	ANF	ANF + DND
q_m (mg g^{-1})	24.39	28.9	34.92	38.73
K_L (L mg^{-1})	2.23	2.17	2.65	3.78
R^2	0.999	0.999	0.999	0.999

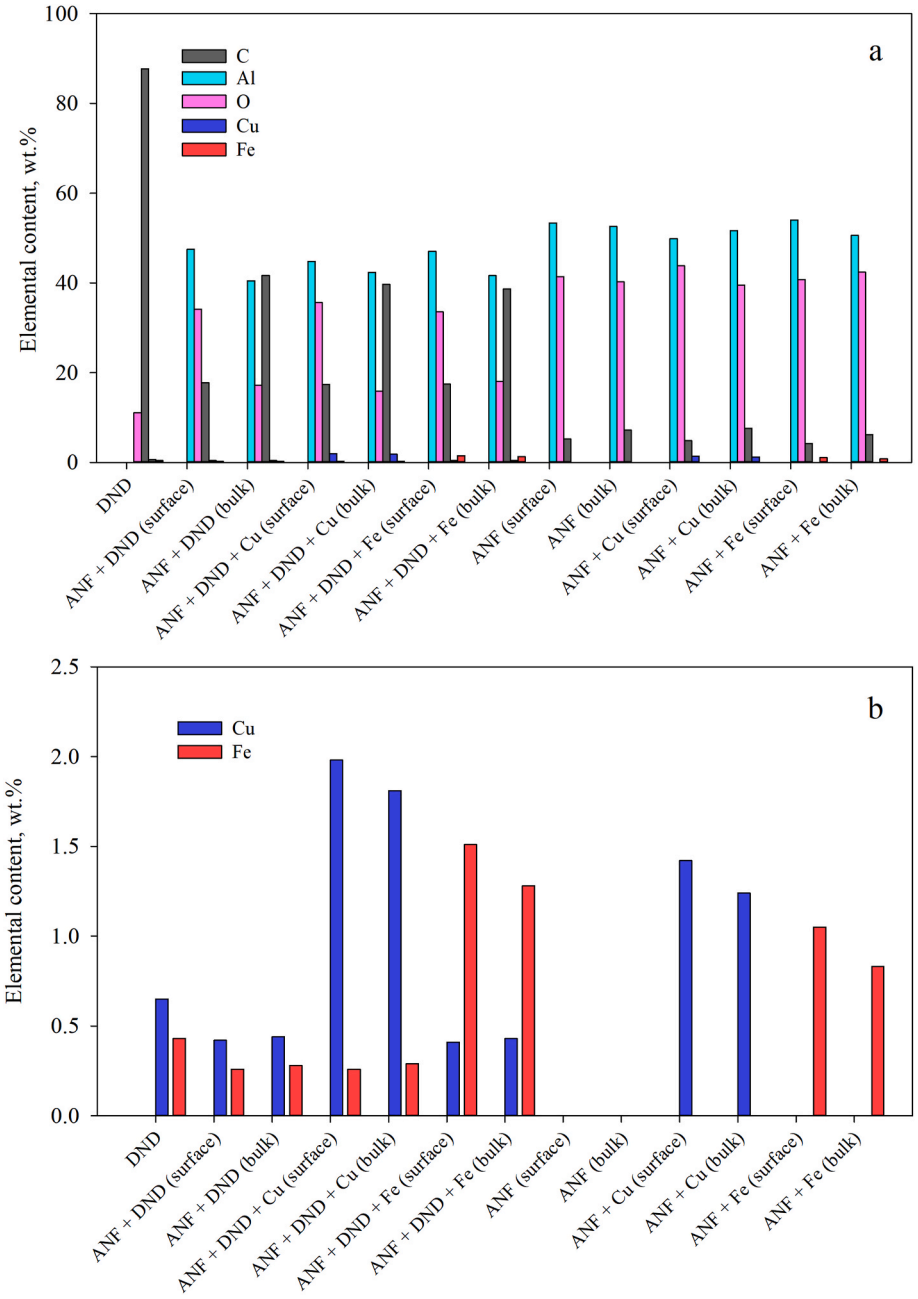

Fig. 5. Elemental analysis of the DND powder, ANF matrix, and ANF + DND composite before and after Cu^{2+} and Fe^{2+} adsorption: overall content (a) and copper and iron content in detail (b).

3.7. FTIR spectroscopy

The Fourier transformed infrared spectra of samples are shown in Fig. 6 (a, b). For the ANF matrix, the broad band at 3447 cm^{-1} corresponds to the stretching vibration of O–H bond, while the bending vibration of this bond is assigned to the peak at 1632 cm^{-1} [62,63]. The three peaks in the range 2800–3000 cm^{-1} belong to the stretching vibrations of C–H bonds in CH_x functional groups [62]. Note that according to the elemental analysis, a small amount of carbon is present in the ANF matrix. The carbonyl group C═O stretching vibration is attributed to the band at 1714 cm^{-1}, while the C–O stretching is assigned to the band at 1076 cm^{-1} [64]. The peak at 1364 cm^{-1} corresponds to the C–OH in-plane bending [64]. Finally, the two peaks at 575 cm^{-1} and 755 cm^{-1} are attributed to the shearing vibrations of Al–O bands in aluminium–oxygen octahedron and tetrahedron, respectively [59].

The adsorption of Cu^{2+} and Fe^{2+} ions on the ANF matrix does not lead to a noticeable change of peak positions except a slight shift of O–H peak from 3447 cm^{-1} to 3437 cm^{-1}. However, we observe the increase O–H band intensity and its widening in the direction of lower wave numbers. It can be expressed in quantitative terms by plotting the integrated intensity of the band from 2210 to 3780 cm^{-1} in Fig. 6 (d). The described transformation of the band after ion adsorption corresponds to a moderate weakening of O–H bonds and formation of more hydrogen bonds in the samples due to complexation reactions (9)–(11). The comparison of integrated intensity for the band from 1490 to 1860 cm^{-1} in Fig. 6 (c) show that it increases in the order ANF + Cu, ANF, ANF + Fe. Thus, it can be supposed that the Cu^{2+} ions are preferably adsorb according to reactions (9) and (10), while the adsorption of the Fe^{2+} ions mainly occurs via reactions (11).

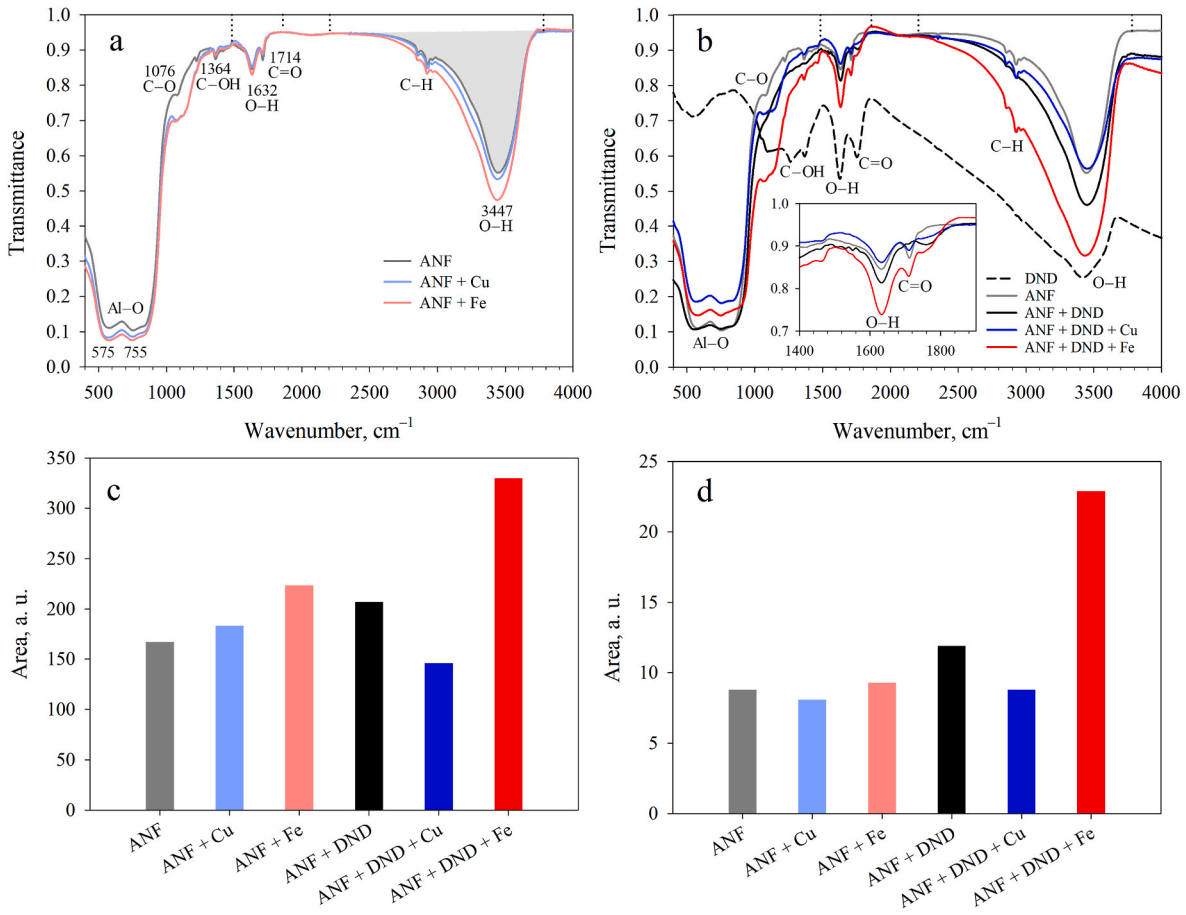

Fig. 6. The measured FTIR spectra of the investigated samples (a, b) and the integrated intensity of bands from 1490 to 1860 cm^{-1} (c) and from 2210 to 3780 cm^{-1} (d). The integrals correspond to the density of area between the measured curve and the straight line connecting two limiting points (as an example, one of the areas for ANF sample is shaded in (a)).

The FTIR spectra of detonation nanodiamonds are shown in Fig. 6 (b). The presence of carboxyl groups on the surface of nanodiamonds (see (8)) results in a very broad band with the peak at 3421 cm^{-1} corresponding to O–H stretching, the peak at 1627 cm^{-1} attributed to O–H bending, and the peak at 1754 cm^{-1} related to C═O stretching. The C═O peak for ANF at 1714 cm^{-1} shifts to 1766 cm^{-1} after formation of ANF + DND composite. The composite material is characterized by a broader and more intense O–H band, which can be also seen by comparison between integrated band intensities of ANF and ANF + DND in Fig. 6 (c, d).

The adsorption of Fe^{2+} ions on the composite leads to a profound broadening of O–H band in the direction of low wave numbers and the increase of its intensity, see Fig. 6 (d). The peak shift from 3450 cm^{-1} to 3436 cm^{-1} is also observed. The interactions between nanofibers/nanodiamonds and metal ions according to complexation reactions (9)–(14) lead to the weakening of O–H bonds and the corresponding frequency/wave number shift. At the same time, the adsorption of Cu^{2+} ions on the composite results in narrowing of O–H band and the decrease of its intensity. A similar trend is observed for the band from 1490 to 1860 cm^{-1}, which integrated characteristics are shown in Fig. 6 (c). These results allow us to conclude that the adsorption of Cu^{2+} ions preferably occurs via reactions (9), (10), and (12), (13), which correspond to breaking of O–H bonds, while the adsorption of Fe^{2+} ions mainly follows reactions (11) and (14). It is interesting to mention the shift of C═O peak for ANF + DND composite at 1766 cm^{-1} to 1711 cm^{-1} after the adsorption of ions. It corresponds to dimerization of carboxyl groups due to formation of hydrogen bonds.

3.8. Catalytic activity

We have studied the catalytic activity of the ANF matrix and ANF + DND composite before and after functionalization in the co-oxidation reaction of phenol with 4-AAP. The activity is evaluated spectrophotometrically as the intensity of optical signal, which is proportional to the amount of colored reaction product. It is found that the functionalization with Cu^{2+} ions increases the catalytic efficiency of the ANF + DND composite by more than two times, and ensures the catalytic activity of the ANF matrix, which initially did not possess such functionality (Fig. 7). The catalytic efficiency of the ANF matrix after adsorption of copper ions is about 90% in comparison with that of the original ANF + DND composite. At the same time, the adsorption of iron ions on the matrix results in extremely low catalytic activity (5–7% of that for copper-activated ANF matrix), and adsorption on the composite leads to a decrease in its initial activity by almost two times. It can be concluded that the most Fe^{2+} ions adsorbed on ANF matrix are not catalytically active, while their adsorption on ANF + DND composite leads to blocking almost half of catalytically active sites on the surface of nanodiamonds resulting in the decrease of composite catalytic activity.

The difference between catalytic activity of samples functionalized by iron and copper ions can be explained on the basis of FTIR spectra results in Section 3.7. We have concluded that the adsorption of Fe^{2+} ions preferably occurs via reactions (11) and (14) and is accompanied by the formation of hydroxide surface groups and hydrogen bonds. These groups can partially block the possibility of oxidation and reduction for Fe^{2+} ions in the Fenton reaction cycle (2). It can explain the poor catalytic performance of samples functionalized by iron ions. Another

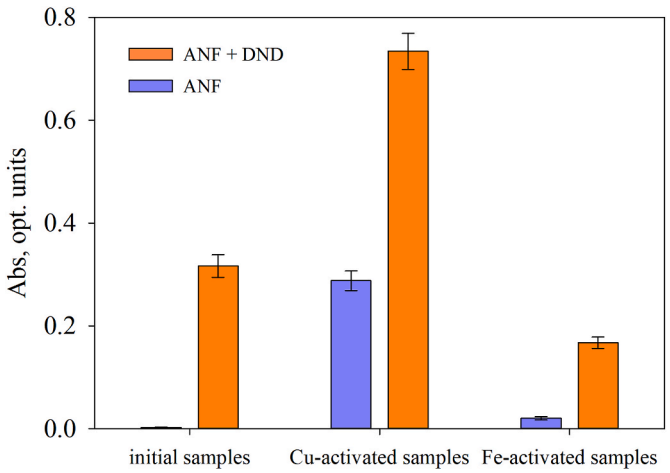

Fig. 7. Catalytic activity of ANF matrix and ANF + DND composite before and after Cu^{2+} and Fe^{2+} adsorption. The phenol concentration in the sample is 200 μM.

reason for that lies in the fact that the Fe^{3+} ions generated in reaction (2) also react with hydroxide ions to form insoluble ferric hydroxide precipitates in neutral and near-neutral pH conditions [48].

The samples functionalized by Cu^{2+} ions contain much smaller surface groups in comparison with ANF + DND and ANF + DND + Fe samples, and the adsorption of ions mainly follows reactions (9) and (12). In this mechanism, the copper ions are only attached to a negatively charged oxygen atom, which apparently leaves the possibility for copper ions to participate in Fenton redox cycle (3). In addition, the Fenton Cu^{2+}/H_2O_2 redox system works over a broader pH range compared to Fe^{2+}/H_2O_2 redox system, which requires the acidic conditions only [48]. It explains the better catalytic activity of Cu-functionalized samples.

Based on the data presented above, the composite functionalized with Cu ions is chosen for studies of its analytical efficiency in the determination of phenol. The results are compared with the original composite as a control. The comparative experiments show that the Cu-activated composite catalyzes the linear formation of reaction product for at least 12 min (Fig. 8). However, in contrast to the original composite, it functions much more efficiently and catalyzes several times

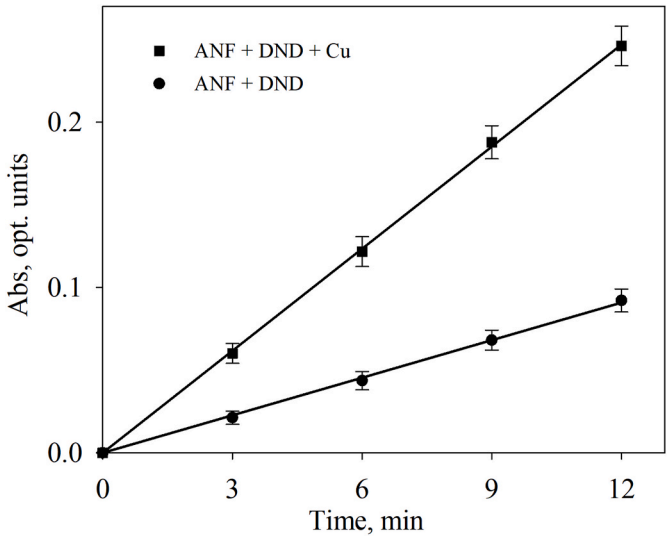

Fig. 8. The dependence of product formation on time for ANF + DND composite before and after functionalization with Cu^{2+} ions. The phenol concentration in the sample is 100 μM.

higher yield of the reaction product. It can be seen from the data in Fig. 8 that in the presence of 100 μM phenol in the test sample, the functionalized composite outputs 3 times more product yield than the control composite under the same conditions. This suggests the advantages of analytical application of functionalized composite in the detection of phenol.

We have shown that ANF + DND composite and ANF + DND + Cu composite provide a linear yield of the color product of the co-oxidation reaction in a wide range of phenol concentrations (0.25–100 μM), see Fig. 9. The same slopes of obtained curves (tg α = 0.0015) indicate the same sensitivity of both sensors to the tested analyte. However, from the data presented in Fig. 9, it can be seen that the ANF + DND + Cu composite catalyzes a significantly higher yield of the product, which makes it possible to detect a two-fold lower analyte concentration (0.25 μM) in contrast to the original composite with the detectable threshold concentration of 0.5 μM. When the phenol concentration in the sample is less than 0.5 μM, the ANF + DND composite catalyzes the formation of an extremely small amount of the colored product, which cannot be reliably determined by the spectral method. The presented data demonstrate the advantages of Cu-activated composite for the detection of phenol in aqueous samples.

Similar results were obtained when evaluating the applicability of the ANF + DND composite and ANF + DND + Cu composite for the determination of 4-chlorophenol. As can be seen from the experimental results in Fig. 10, both sensors provide a linear yield of the colored product of the co-oxidation reaction in a wide range of 4-chlorophenol concentrations (0.5–25 μM). The Cu-activated composite makes it possible to detect a two-fold lower concentration of 4-chlorophenol (0.5 μM) in comparison with the original composite with the threshold concentration of 1 μM.

The comparison of analytical performance of ANF + DND + Cu composite to a number of others sensors described in the literature is presented in Table 3. The proposed sensor provides the widest range of analyte concentration with the linear response (LR) and the lowest limit of detection (LOD). The only exception is the conductometric biosensor, which has the upper detection limit of 3187 μM and the lower limit of 10 μM, which is still much higher in comparison with the proposed sensor. For 4-chlorophenol, our sensor has a fairly wide range of determined analyte concentrations and a satisfactory value of LOD.

In model experiments, we demonstrated the applicability of ANF + DND and ANF + DND + Cu composites as reusable sensors for repeated testing of phenol in an aqueous medium. As can be seen from the obtained data, both composites provide almost the same yield of the oxidative azo coupling reaction product in a series of five consecutive tests of water samples with the same phenol concentration (Fig. 11). The obtained results demonstrate that the catalytic efficiency of Cu-activated composite is two times higher than that of the original composite. It is important to note that after each measurement, both composites are washed three times with DI water to remove residual components and the reaction product. It testifies to the strong binding of Cu^{2+} ions to the composite, which are not eluted and are not inactivated upon interaction with the reagents during repeated determination of the analyte.

4. Conclusion

We have investigated the effect of adsorption of iron and copper ions on the catalytic activity of alumina nanofiber (ANF) matrix and the composite material based on alumina nanofibers and detonation nanodiamonds (DND) in the co-oxidation of phenols with 4-aminoantipyrine in the presence of hydrogen peroxide. It is found that the adsorption kinetics is described by the pseudo-first-order model and the adsorption equilibrium data follow the Langmuir isotherm. It suggests that the ions are adsorbed on the surface of ANF matrix or ANF + DND composite in the form of a monolayer interacting their functional groups. The incorporation of DND nanoparticles into the ANF matrix increases its sorption capacity by 12–15%. We have found more than two-fold

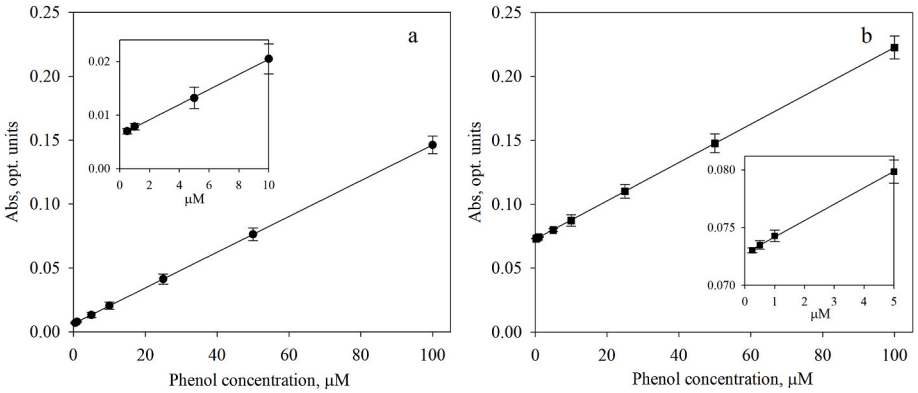

Fig. 9. The response curve of ANF + DND composite (a) and ANF + DND + Cu composite (b) towards different concentrations of phenol.

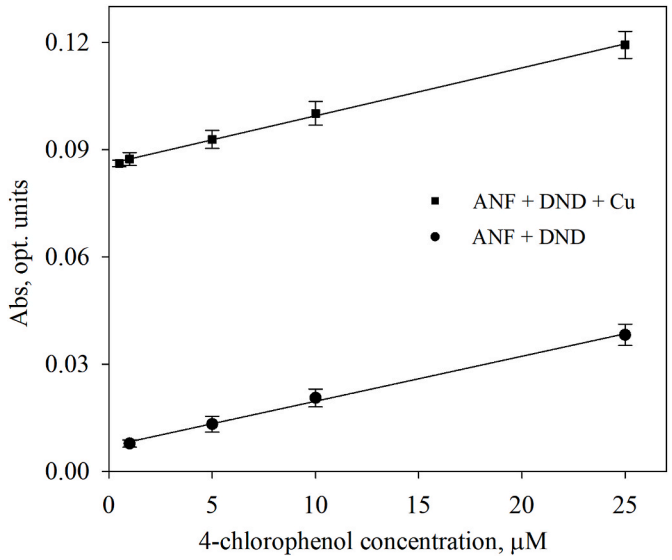

Fig. 10. The response curve of ANF + DND composite before and after functionalization with Cu^{2+} ions towards different concentrations of 4-chlorophenol.

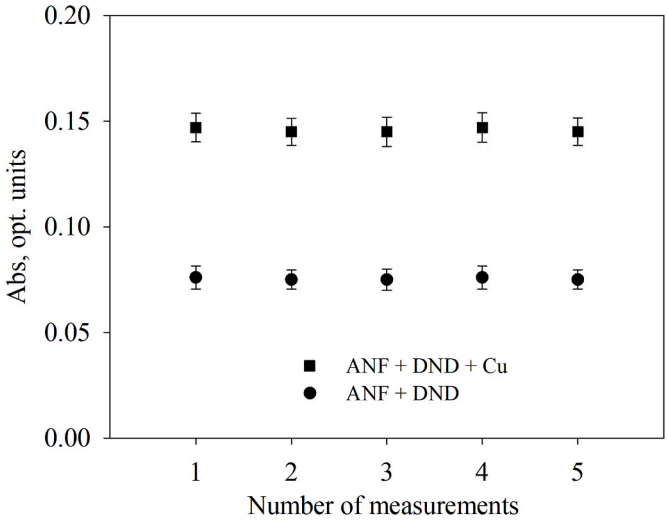

Fig. 11. The results of successive tests of the ANF + DND and ANF + DND + Cu composites in aqueous samples with equal phenol concentration (100 μM).

Table 3
Comparison in analytical performance of ANF + DND + Cu sensor with other reported sensors for phenol and 4-clorophenol detection.

Sensors based on different composites	Phenol		4-chlorophenol	
	LR (μM)	LOD (μM)	LR (μM)	LOD (μM)
ANF + DND + Cu composite (Present work)	0.25–100	0.25	0.5–25	0.5
Fe_3O_4 NPs based sensor [31]	1–15	1.0	–	–
CuO NPs based sensor [33]	0.25–2.5	0.69	0.25–1	0.43
HRP/Au/GCE [65]	–	–	2.5–40	0.39
Tyrosinase/chitosan film [66]	2.5–70.0	1.0	2.5–50.0	0.9
Bacterial strain-based conductometric biosensor [67]	10–3187	2	–	–
PGEs/DTAB electrochemical sensor [68]	10–50	1.2	–	–

increase of the catalytic activity for ANF + DND + Cu composite, while the activity of ANF + DND + Fe composite is found to decrease by several times in comparison with the original ANF + DND material. The results of FTIR analysis indicate that the adsorption of iron ions occurs with the formation of hydroxide surface groups and hydrogen bonds, which apparently block their catalytic activity in the Fenton redox cycle. At the same time, the copper ions are attached to a negatively charged oxygen atoms, which apparently leaves the possibility for copper ions to participate in the redox cycle.

Functionalization of the ANF + DND composite with Cu^{2+} ions significantly increases its catalytic efficiency in the co-oxidation reaction of phenolic compounds with 4-aminoantipyrine, which make it possible to detect two times lower concentrations of these analytes compared to the original composite. It is shown that the functionalized composite provides a linear yield of the co-oxidation reaction product in a wide range of analyte concentrations: 0.25–100 μM for phenol and 0.5–25 μM for 4-chlorophenol. Model experiments demonstrate the applicability of ANF + DND + Cu composite as a reusable sensor for the determination of phenol in aqueous samples.

CRediT authorship contribution statement

Nikita O. Ronzhin: Conceptualization, Formal analysis, Investigation, Methodology, Visualization, Writing – original draft, Writing – review & editing. **Ekaterina D. Posokhina:** Formal analysis, Investigation, Methodology. **Elena V. Mikhlina:** Investigation, Methodology. **Nikolai P. Shestakov:** Investigation, Methodology. **Ivan V. Nemtsev:** Investigation. **Vladimir S. Bondar:** Writing – review & editing, Supervision. **Ilya I. Ryzhkov:** Conceptualization, Formal analysis, Methodology, Writing – review & editing, Supervision, Project administration.

Declaration of competing interest

The authors declare that they have no known competing financial interests or personal relationships that could have appeared to influence the work reported in this paper.

Acknowledgements

This work is supported by the Russian Foundation for Basic Research, Project 18–29–19078. The authors would like to express their special thanks to Krasnoyarsk Regional Center of Research Equipment of Federal Research Center « Krasnoyarsk Science Center SB RAS » for providing the equipment to ensure the accomplishment of this project.

References

[1] J. Michałowicz, W. Duda, Phenols – sources and toxicity, Pol. J. Environ. Stud. 16 (2007) 347–362.
[2] M.Y. Ghaly, G. Härtel, R. Mayer, R. Haseneder, Photochemical oxidation of p-chlorophenol by UV/H_2O_2 and photo-Fenton process. A comparative study, J. Waste Manag. 21 (2001) 41–47, https://doi.org/10.1016/s0956-053x(00)00070-2.
[3] C. Guillard, J. Disdier, C. Monnet, J. Dussaud, S. Malato, J. Blanco, M. I. Maldonado, J.M. Herrmann, Solar efficiency of a new deposited titania photocatalyst: chlorophenol, pesticide and dye removal applications, Appl. Catal. 46 (2003) 319–332, https://doi.org/10.1016/S0926-3373(03)00264-9.
[4] K. Abburi, Adsorption of phenol and p-chlorophenol from their single and bisolute aqueous solutions on Amberlite XAD-16 resin, J. Hazard Mater. 105 (2003) 143–156, https://doi.org/10.1016/j.jhazmat.2003.08.004.
[5] F.A. Banat, B. Al-Bashir, S. Al-Asheh, O. Hayajneh, Adsorption of phenol by bentonite, Environ. Pollut. 107 (2000) 391–398, https://doi.org/10.1016/S0269-7491(99)00173-6.
[6] W.W. Anku, M.A. Mamo, P.P. Govender, Phenolic compounds in water: sources, reactivity, toxicity and treatment methods, chapter 17, in: M. Soto-Hernández (Ed.), Phenolic Compounds: Natural Sources, Importance and Applications, InTechOpen, London, 2017, https://doi.org/10.5772/66927.
[7] A.M. Hammam, M.S. Zaki, R.A. Yousef, O. Fawzi, Toxicity, Mutagenicity and carcinogenicity of phenols and phenolic compounds on human and living organisms (A Review), Adv. Environ. Biol. 9 (2015) 38–48.
[8] B.K. Bernard, A.M. Hoberman, A study of the developmental toxicity potential of pentachlorophenol in the rat, Int. J. Toxicol. 20 (2001) 353–362, https://doi.org/10.1080/109158101753333631.
[9] Criteria and standard division office of water planning and standard U.S. Environmental protection agency, Washington, D.C. Phenol, ambient water quality Criteria. http://nepis.epa.gov/Exe/ZyPDF.cgi/9100H4VJ.PDF?Dockey=9100H4VJ.PDF, 1978.
[10] European union risk assessment report. Phenol. 1st priority list, European chemicals bureau, Germany. https://op.europa.eu/en/publication-detail/-/publication/f9f7cfc6-ffc1-4284-a6a5-96e5ba34f391, 2006, 64.
[11] P. Ramakrishnan, K. Rangiah, A UHPLC-MS/SRM method for analysis of phenolics from Camellia sinensis leaves from Nilgiri hills, Anal. Methods 8 (2016) 8033–8041, https://doi.org/10.1039/C6AY02329K.
[12] L.N. Moskvin, O.V. Rodinkov, A.L. Moskvin, V. Spivakovskii, A.Y. Vlasov, A. S. Bugaichenko, A.S. Samokhin, P.N. Nesterenko, Chromatomembrane preconcentration of phenols using a new 3D printed microflow cell followed by reversed-phase HPLC determination, J. Separ. Sci. 44 (2021) 2449–2456, https://doi.org/10.1002/jssc.202100089.
[13] Z. Li, Y. Yue, Y. Hao, S. Feng, X. Zhou, A glassy carbon electrode modified with cerium phosphate nanotubes for the simultaneous determination of hydroquinone, catechol and resorcinol, Microchim. Acta 185 (2018) 215, https://doi.org/10.1007/s00604-018-2748-z.
[14] M. Baghayeri, A. Amiri, M. Fayazi, M. Nodehi, A. Esmaeelnia, Electrochemical detection of bisphenol a on a MWCNTs/$CuFe_2O_4$ nanocomposite modified glassy carbon electrode, Mater. Chem. Phys. 261 (2021) 12424, https://doi.org/10.1016/j.matchemphys.2021.124247.
[15] T.S.S.K. Naik, A.V. Kesavan, B.E.K. Swamy, S. Singh, A.G. Anil, V. Madhavi, P. C. Ramamurthy, Low cost, trouble-free disposable pencil graphite electrode sensor for the simultaneous detection of hydroquinone and catechol, Mater. Chem. Phys. 278 (2022) 125663, https://doi.org/10.1016/j.matchemphys.2021.125663.
[16] S.L. Fan, L.K. Zhang, J.M. Lin, Post-column detection of benzenediols and 1,2,4-benzenetriol based on acidic potassium permanganate chemiluminescence, Talanta 68 (2006) 646–652, https://doi.org/10.1016/j.talanta.2005.05.004.
[17] Y. Liu, Y.M. Wang, W.Y. Zhu, C.H. Zhang, H. Tang, J.H. Jiang, Conjugated polymer nanoparticles-based fluorescent biosensor for ultrasensitive detection of hydroquinone, Anal. Chim. Acta 1012 (2018) 60–65, https://doi.org/10.1016/j.aca.2018.01.027.
[18] R. Tabaraki, E. Heidarizadi, Spectrophotometric determination of phenol and chlorophenols by salting out assisted liquid-liquid extraction combined with dispersive liquid-liquid microextraction, Spectrochim. Acta: Mol. Biomol. Spectrosc. 215 (2019) 405–409, https://doi.org/10.1016/j.saa.2019.02.060.
[19] J.Q. Xu, Q.L. Sheng, Y. Shen, J.B. Zheng, Enhanced direct electron transfer of glucose oxidase based on gold nanoprism and its application in biosensing, Colloids Surf. A Physicochem. Eng. Asp. 529 (2017) 113–118, https://doi.org/10.1016/j.colsurfa.2017.05.049.
[20] R. Rahmanian, S.A. Mozaffari, Electrochemical fabrication of ZnO-polyvinyl alcohol nanostructured hybrid film for application to urea biosensor, Sensor. Actuator. B Chem. 207 (2015) 772–781, https://doi.org/10.1016/j.snb.2014.10.129.
[21] S. Soylemez, F.E. Kanik, M. Ileri, S.O. Hacioglu, L. Toppare, Development of a novel biosensor based on a conducting polymer, Talanta 118 (2014) 84–89, https://doi.org/10.1016/j.talanta.2013.10.007.
[22] C.J. Mao, X.B. Chen, H.L. Niu, J.M. Song, S.Y. Zhang, R.J. Cui, A novel enzymatic hydrogen peroxide biosensor based on Ag/C nanocables, Biosens. Bioelectron. 31 (2012) 544–547, https://doi.org/10.1016/j.bios.2011.10.001.
[23] A. Baral, L. Satish, S.K. Padhy, D.P. Das, S. Ju, M.K. Ghosh, Structure and activity of lysozyme on binding to lithium-manganese oxide nanocomposites prepared from seabed nodule, J. Phys. Chem. Solid. 151 (2021), https://doi.org/10.1016/j.jpcs.2020.109794, 109794.
[24] L. Gao, J. Zhuang, L. Nie, J. Zhang, Y. Zhang, G. Ning, T. Wang, J. Feng, D. Yang, S. Perrett, X. Yan, Intrinsic peroxidase-like activity of ferromagnetic nanoparticles, Nat. Nanotechnol. 2 (2007) 577–583, https://doi.org/10.1038/nnano.2007.260.
[25] W. He, Y. Liu, J. Yuan, J.J. Yin, X. Wu, X. Hu, K. Zhang, J. Liu, C. Chen, Y. Ji, Y. Guo, Au@Pt nanostructures as oxidase and peroxidase mimetics for use in immunoassays, Biomaterials 32 (2011) 1139–1147, https://doi.org/10.1016/j.biomaterials.2010.09.040.
[26] A. Asati, S. Santra, C. Kaittanis, S. Nath, J.M. Perez, Oxidase-like activity of polymer-coated cerium oxide nanoparticles, Angew. Chem. Int. Ed. 48 (2009) 2308–2312, https://doi.org/10.1002/anie.200805279.
[27] Y.J. Long, Y.F. Li, Y. Liu, J.J. Zheng, J. Tang, C.J. Huang, Visual observation of the mercury-stimulated peroxidase mimetic activity of gold nanoparticles, Chem. Commun. 47 (2011) 11939–11941, https://doi.org/10.1039/C1CC14294A.
[28] W. Chen, J. Chen, Y.B. Feng, L. Hong, Q.Y. Chen, L.F. Wu, X.H. Lin, X.H. Xia, Peroxidase-like activity of water-soluble cupric oxide nanoparticles and its analytical application for detection of hydrogen peroxide and glucose, Analyst 137 (2012) 1706–1712, https://doi.org/10.1039/C2AN35072F.
[29] Y. Song, K. Qu, C. Zhao, J. Ren, X. Qu, Graphene oxide: intrinsic peroxidase catalytic activity and its application to glucose detection, Adv. Mater. 22 (2010) 2206–2210, https://doi.org/10.1002/adma.200903783.
[30] Y. Song, X. Wang, C. Zhao, K. Qu, J. Ren, X. Qu, Label-free colorimetric detection of single nucleotide polymorphism by using single-walled carbon nanotube intrinsic peroxidase-like activity, Chem.—A Eur. J. 16 (2010) 3617–3621, https://doi.org/10.1002/chem.200902643.
[31] P. Chandane, J. Ladke, C. Jori, S. Deshmukh, S. Zinjarde, M. Chakankar, H. Hocheng, U. Jadhav, Synthesis of magnetic Fe_3O_4 nanoparticles from scrap iron and use of their peroxidase like activity for phenol detection, J. Environ. Chem. Eng. 7 (2019) 103083, https://doi.org/10.1016/j.jece.2019.103083.
[32] M. Nurdin, L. Agusu, A.A.M. Putra, M. Maulidiyah, Z. Arham, D. Wibowo, M. Z. Muzakkar, A.A. Umar, Synthesis and electrochemical performance of graphene-TiO_2-carbon paste nanocomposites electrode in phenol detection, J. Phys. Chem. Solid. 131 (2019) 104–110, https://doi.org/10.1016/j.jpcs.2019.03.014.
[33] J. Du, S. Qi, T. Fan, Y. Yang, C. Wang, Q. Shu, S. Zhuo, C. Zhu, Nitrogen and copper-doped carbon quantum dots with intrinsic peroxidase-like activity for double-signal detection of phenol, Analyst 146 (2021) 4280–4289, https://doi.org/10.1039/D1AN00796C.
[34] F. Pino, C.C. Mayorga-Martinez, A. Merkoçi, High-performance sensor based on copper oxide nanoparticles for dual detection of phenolic compounds and a pesticide, Electrochem. Commun. 71 (2016) 33–37, https://doi.org/10.1016/j.elecom.2016.08.001.
[35] A. Scroccarello, F. Della Pelle, D. Rojas, G. Ferraro, E. Fratini, S. Gaggiotti, A. Cichelli, D. Compagnone, Metal nanoparticles based lab-on-paper for phenolic compounds evaluation with no sample pretreatment. Application to extra virgin olive oil samples, Anal. Chim. Acta 1183 (2021) 338971, https://doi.org/10.1016/j.aca.2021.338971.
[36] L. Jiang, I. Santiago, J. Foord, Nanocarbon and nanodiamond for high performance phenolics sensing, Commun. Chem. 1 (2018) 43, https://doi.org/10.1038/s42004-018-0045-8.
[37] L. Jiang, I. Santiago, J. Foord, A comparative study of fouling-free nanodiamond and nanocarbon electrochemical sensors for sensitive bisphenol A detection, Carbon 174 (2021) 390–395, https://doi.org/10.1016/j.carbon.2020.11.073.
[38] L. Bian, H. Zong, C. Li, J. Zang, Y. Wang, D. Zhang, Y. Li, Amperometric determination of hydroquinone and catechol based on nanodiamond powder electrode, Int. J. Electrochem. Sci. 14 (2019) 186–195, https://doi.org/10.20964/2019.01.61.
[39] J.R. Camargo, M. Baccarin, P.A. Raymundo-Pereira, A.M. Campos, G.G. Oliveira, O. Fatibello-Filho, O.N. Oliveira, B.C. Janegitz, Electrochemical biosensor made with tyrosinase immobilized in a matrix of nanodiamonds and potato starch for detecting phenolic compounds, Anal. Chim. Acta 1034 (2018) 137–143, https://doi.org/10.1016/j.aca.2018.06.001.
[40] N.O. Ronzhin, A.P. Puzyr, V.S. Bondar, Detonation nanodiamonds as a new tool for phenol detection in aqueous medium, J. Nanosci. Nanotechnol. 18 (2018) 5448–5453, https://doi.org/10.1166/jnn.2018.15382.
[41] N.O. Ronzhin, E.D. Posokhina, E.V. Mikhlina, Y.L. Mikhlin, M.M. Simunin, L. S. Tarasova, S.A. Vorobyev, V.S. Bondar, I.I. Ryzhkov, A new composite material based on alumina nanofibers and nanodiamonds: synthesis, characterization, and sensing application, J. Nanoparticle Res. 23 (2021) 199, https://doi.org/10.1007/s11051-021-05309-y.

[42] M. Kutuzov, Method and System for Alumina Nanofibers Synthesis from Molten Aluminum, US Patent, 2013. №2013/0192517 A1.
[43] M. Aghayan, I. Hussainova, M. Kutuzov, M. Friman, Coupled thermal analysis of novel alumina nanofibers with ultrahigh aspect ratio, Thermochim. Acta 574 (2013) 140–144, https://doi.org/10.1016/j.tca.2013.10.010.
[44] V.M.T. Su, T.W. Clyne, Hybrid filtration membranes incorporating nanoporous silica within a nanoscale alumina fiber scaffold, Adv. Eng. Mater. 18 (2016) 96–104, https://doi.org/10.1002/adem.201500220.
[45] A.P. Puzyr, V.S. Bondar, Method of Production of Nanodiamonds of Explosive Synthesis with an Increased Colloidal Stability, 2005. RU Patent № 2252192.
[46] S. Hussain, E. Aneggi, D. Goi, Catalytic activity of metals in heterogeneous Fenton-like oxidation of wastewater contaminants: a review, Environ. Chem. Lett. 19 (2021) 2405–2424, https://doi.org/10.1007/s10311-021-01185-z.
[47] A.N. Pham, G. Xing, C.J. Miller, T.D. Waite, Fenton-like copper redox chemistry revisited: hydrogen peroxide and superoxide mediation of copper-catalyzed oxidant production, J. Catal. 301 (2013) 54–64, https://doi.org/10.1016/j.jcat.2013.01.025.
[48] A.D. Bokare, W. Choi, Review of iron-free Fenton-like systems for activating H_2O_2 in advanced oxidation processes, J. Hazard Mater. 275 (2014) 121–135, https://doi.org/10.1016/j.jhazmat.2014.04.054.
[49] H.Y. Kim, H.J. Lee, S.K. Chang, Reaction-based colorimetric signaling of Cu^{2+} ions by oxidative coupling of phenols with 4-aminoantipyrine, Talanta 132 (2015) 625–629, https://doi.org/10.1016/j.talanta.2014.09.048.
[50] J.A. Nicell, H. Wright, A model of peroxidase activity with inhibition by hydrogen peroxide, Enzym. Microb. Technol. 21 (1997) 302–310, https://doi.org/10.1016/S0141-0229(97)00001-X.
[51] M.B. McBride, Cu^{2+}-Adsorption characteristics of aluminum hydroxide and oxyhydroxides, Clay Clay Miner. 30 (1982) 21–28, https://doi.org/10.1346/CCMN.1982.0300103.
[52] S.S. Gupta, K.G. Bhattacharyya, Kinetics of adsorption of metal ions on inorganic materials: a review, Adv. Colloid Interface Sci. 162 (2011) 39–58, https://doi.org/10.1016/j.cis.2010.12.004.
[53] J.A. Davis, R.O. James, J.O. Leckie, Surface ionization and complexation at the oxide/water interface: I. Computation of electrical double layer properties in simple electrolytes, J. Colloid Interface Sci. 63 (1978) 480–499, https://doi.org/10.1016/S0021-9797(78)80009-5.
[54] R. Sprycha, Electrical double layer at alumina/electrolyte interface: I. Surface charge and zeta potential, J. Colloid Interface Sci. 127 (1989) 1–11, https://doi.org/10.1016/0021-9797(89)90002-7.
[55] R. Sprycha, Electrical double layer at alumina/electrolyte interface. II. Adsorption of supporting electrolyte ions, J. Colloid Interface Sci. 127 (1989) 12–25, https://doi.org/10.1016/0021-9797(89)90003-9.
[56] P. Stenclova, V. Celedova, A. Artemenko, V. Jirasek, J. Jira, B. Rezek, A. Kromka, Surface chemistry of water-dispersed detonation nanodiamonds modified by atmospheric DC plasma afterglow, RSC Adv. 7 (2017) 38973–38980, https://doi.org/10.1039/C7RA04167E.
[57] D.G. Lim, K.H. Kim, E. Kang, S.H. Lim, J. Ricci, M.T. Kwon, S.H. Jeong, Comprehensive evaluation of carboxylated nanodiamond as a topical drug delivery system, Int. J. Nanomed. 11 (2016) 2381–2395, https://doi.org/10.2147/IJN.S104859.
[58] R. Hana, W. Zoua, Z. Zhang, J. Shi, J. Yang, Removal of copper (II) and lead (II) from aqueous solution by manganese oxide coated sand: I. Characterization and kinetic study, J. Hazard Mater. 137 (2006) 384–395, https://doi.org/10.1016/j.jhazmat.2006.02.021.
[59] R. Wang, W. Zhang, L. Zhang, T. Hua, G. Tang, X. Peng, M. Hao, Q. Zuo, Adsorption characteristics of Cu(II) and Zn(II) by nano-alumina material synthesized by the sol-gel method in batch mode, Environ. Sci. Pollut. Res. 26 (2019) 1595–1605, https://doi.org/10.1007/s11356-018-3453-5.
[60] Y. Ren, N. Yanc, J. Feng, J. Mab, Q. Wen, N. Li, Q. Dong, Adsorption mechanism of copper and lead ions onto graphene nanosheet/δ-MnO_2, Mater. Chem. Phys. 136 (2012) 538–544, https://doi.org/10.1016/j.matchemphys.2012.07.023.
[61] C. Du, H. Liu, M. Xiao, D. Gao, D. Huang, Z. Li, T. Chen, J. Mo, K. Wang, C. Zhang, Adsorption of iron and lead ions from an aqueous solution by plasma-modified activated carbon, Ind. Eng. Chem. Res. 51 (2012) 15618–15625, https://doi.org/10.1021/ie302011n.
[62] V.S. Solodovnichenko, D.V. Lebedev, V.V. Bykanova, A.V. Shiverskiy, M. M. Simunin, V.A. Parfenov, I.I. Ryzhkov, Carbon coated alumina nanofiber membranes for selective ion transport, Adv. Eng. Mater. 19 (2017) 1700244, https://doi.org/10.1002/adem.201700244.
[63] H.A. Dabbagh, M. Yalfani, B.H. Davis, An XRD and Fourier-transformed infrared spectroscopy investigation of single and mixed γ-alumina and thorium oxide, J. Mol. Catal. Chem. 238 (2005) 72–77, https://doi.org/10.1016/j.molcata.2005.03.037.
[64] D. Lin-Vien, N.B. Colthup, W.G. Fateley, J.G. Grasselli, The Handbook of Infrared and Raman Characteristic Frequencies of Organic Molecules, first ed., Academic Press, London, 1991.
[65] C. Qiu, T. Chen, X. Wang, Y. Li, H. Ma, Application of horseradish peroxidase modified nanostructured Au thin films for the amperometric detection of 4-chlorophenol, Colloids Surf., B 103 (2013) 129–135, https://doi.org/10.1016/j.colsurfb.2012.10.017.
[66] J. Abdullah, M. Ahmad, N. Karuppiah, L.Y. Heng, H. Sidek, Immobilization of tyrosinase in chitosan film for an optical detection of phenol, Sensor. Actuator. B Chem. 114 (2006) 604–609, https://doi.org/10.1016/j.snb.2005.06.019.
[67] N. Kolahchia, M. Braiekb, G. Ebrahimipoura, S.O. Ranaei-Siadatc, F. Lagarde, N. Jaffrezic-Renault, Direct detection of phenol using a new bacterial strain-based conductometric biosensor, J. Environ. Chem. Eng. 6 (2018) 478–484, https://doi.org/10.1016/j.jece.2017.12.023.
[68] G. Congur, U.D. Gül, Phenol monitoring in water samples using an inexpensive electrochemical sensor based on pencil electrodes modified with DTAB surfactant, J. Environ. Chem. Eng. 9 (2021) 105804, https://doi.org/10.1016/j.jece.2021.105804.